Theor. Comput. Fluid Dyn. (2012) 26:361–379
DOI 10.1007/s00162-011-0238-6

ORIGINAL ARTICLE

Yechun Wang · Panagiotis Dimitrakopoulos

Low-Reynolds-number droplet motion in a square microfluidic channel

Received: 18 February 2011 / Accepted: 5 July 2011 / Published online: 22 July 2011

Abstract In this study, we investigate computationally the low-Reynolds-number droplet motion in a square micro-channel, a problem frequently encountered in microfluidic devices, enhanced oil recovery and coating processes. The droplet deformation and motion are determined via a three-dimensional spectral boundary element method for wall-bounded flows. The effects of the flow rate, viscosity ratio and droplet size on the interfacial dynamics are identified for droplets smaller and larger than the channel size and for a wide range of viscosity ratio. Owing to the stronger hydrodynamic forces in the thin lubrication film between the droplet interface and the solid walls, large droplets exhibit larger deformation and smaller velocity. Under the same average velocity, a droplet in a channel shows a significantly smaller deformation and higher velocity than in a cylindrical tube with the same size, owing to the existence of the corners' area in the channel which permits flow of the surrounding fluid. A suitable periodic boundary implementation for our spectral element method is developed to study the dynamics of an array of identical droplets moving in the channel. In this case, the droplet deformation and velocity are reduced as their separation decreases; the reduction is influenced by the flow rate, viscosity ratio and more significantly the droplet size.

Keywords Droplet motion · Low-Reynolds-number flow · Microfluidics · Spectral boundary element method

1 Introduction

Studies on the deformation and migration of neutrally buoyant droplets in micro-channels are intrigued by the recent development of microfluidic devices. For example, micro-channels are employed for droplet sorting and fission [6,17,30]. Droplets moving in microfluidic channels are utilized as "micro-reactors" in order to control chemical reactions on the milli-second scale [29,31]. Besides microfluidics, understanding the behavior of non-wetting droplets in micro-channels is also of great importance for other industrial processes. In the lubrication process, lubricants usually contain a small amount of immersed bubbles altering the performance of journal bearings and squeezing film dampers [27]. In enhanced oil recovery, foam is generated within the underground porous media to displace the oil [21]. An accurate estimation of the wetting film thickness between droplets composing the foam and the pore wall is desired in order to predict the percentage of recoverable oil. In the coating process, the wetting film thickness is also a direct measure of the coating load for coating the inner surface of monolithic channels [15,16]. The fundamental physics of bubble behavior in micro-channels is also

Communicated by: Eldredge.

Y. Wang (✉)
Department of Mechanical Engineering, North Dakota State University, Fargo, ND 58108, USA
E-mail: yechun.wang@ndsu.edu

P. Dimitrakopoulos
Department of Chemical and Biomolecular Engineering, University of Maryland, College Park, MD 20742, USA

essential in the operation and design of fuel cells, e.g. , the removal of CO_2 bubbles in the anode channel of a direct methanol fuel cell (DMFC) [18].

A plethora of studies has investigated the motion of droplets/bubbles in cylindrical tubes, including studies for long droplets with an open upstream end [1–3,7,8,12,25,28] and for droplets with size comparable to the tube radius [4,11,19,22,33]. However, droplet behavior in non-axisymmetric (i.e., square, rectangular or elliptic) capillaries has received less attention, although those capillaries are encountered in numerous applications and may be employed as better models to describe the irregular and angular nature of porous media [16,38].

Most studies on droplet dynamics in channels focused on the motion of highly elongated bubbles (with a size much larger than the dimension of the channel's cross-section) or air fingers (long bubbles with their upstream end open). Ransohoff and Radke [24] investigated the motion of a long bubble or droplet in a constricted non-circular capillary. Ratulowski and Chang [25] studied the motion of a neutrally buoyant long bubble pushed with a constant velocity through a straight non-circular capillary. Lubrication analysis was employed to compute the pressure drop and wetting film thickness for a single bubble and an array of bubbles moving in a square channel. Kolb and Cerro [15,16] conducted both experimental studies and lubrication analysis on the motion of an air finger in a square channel. Thulasidas et al. [32] later augmented Kolb and Cerro's experiments by including the investigation of bubble-train flow in square channels. Wong et al. [38,39] determined the pressure–velocity relation for a long bubble moving in polygonal channels in the limit of negligible capillary number Ca. By employing a finite element analysis, Hazel and Heil [10] extended Wong etal's study [38,39] to include cases with $Ca = O(1)$ for square channels. They also investigated the steady motion of a long bubble in both rectangular and elliptical channels. Mortazavi and Tryggvason [20] considered the droplet motion in a square channel via a finite difference/front tracking method. The authors determined the effects of viscosity ratio, capillary number and Reynolds number for droplets smaller than the channel size. Sarrazin et al. [26] determined, via two- and three-dimensional computations, the droplet deformation and velocity field inside both the droplet and the surrounding fluid for droplet motion in rectangular micro-channels. The droplet dynamics between two parallel plates has also been investigated recently [9,13,14].

In this work, we consider the motion of droplets moving in a micro-channel with a square cross-section. A three-dimensional spectral boundary element method is employed to study the dynamics of droplets comparable to (i.e., smaller and larger than) the channel size. The interest in this investigation results from the fact that droplets with comparable size to the channel size are frequently encountered in microfluidic and enhanced oil recovery. We first study the deformation and motion of a single droplet as a function of the flow rate (or capillary number), viscosity ratio and droplet size. Then, the motion of an array of identical droplets in the square channel is investigated by employing periodic boundary conditions. The results of this study may provide useful insight into the operation and design of microfluidic devices for foam generation and droplet sorting.

2 Mathematical formulation and computational method

2.1 Droplet motion in a micro-channel

As shown in Fig. 1, we consider the motion of a neutrally buoyant droplet (fluid 1) with viscosity $\lambda\mu$ and density ρ_1 surrounded by another immiscible fluid (fluid 2) with viscosity μ and density $\rho_2 = \rho_1$ in a square channel with a width comparable to the droplet size. The surface tension γ is assumed constant over the droplet interface. The characteristic size of the droplet is $\tilde{a} = (3V/4\pi)^{1/3}$, where V is the droplet volume. The size of the channel, i.e., the half-width of the cross-section, is denoted as R. The droplet velocity in the flow direction U_x may be different than the average velocity U in the channel. In this study, we investigate the behavior of droplets moving along the channel centerline; therefore, there is no cross-stream droplet migration taking place, i.e., the droplet velocity in the direction of the y- and z-axes is always zero due to the symmetry.

The steady unidirectional flow in the square channel far from the droplet is given by [40]

$$\frac{u_x^\infty}{C} = \left(R^2 - z^2\right) + \sum_{n=1}^{\infty} B_n \cosh\left(\frac{\alpha_n y}{R}\right) \cos\left(\frac{\alpha_n z}{R}\right) \tag{1}$$

where

$$C = \frac{-(\mathrm{d}p/\mathrm{d}x)}{2\mu}, \qquad B_n \cosh(\alpha_n) = (-1)^n \frac{4R^2}{\alpha_n^3}, \qquad \alpha_n = \frac{(2n-1)\pi}{2} \tag{2}$$

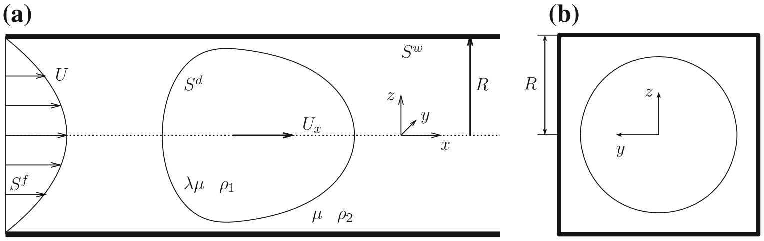

Fig. 1 Illustration of a droplet moving along the centerline of a square micro-channel. The geometry is shown at **a** the xz-plane and **b** the yz-plane

The flow rate Q in the channel may be derived as

$$\frac{Q}{C} = \frac{8R^4}{3} + \sum_{n=1}^{\infty} B_n \left(\frac{2R}{\alpha_n}\right)^2 \sinh(\alpha_n)\sin(\alpha_n) \tag{3}$$

while the undisturbed average velocity in the channel is $U = Q/(4\,R^2)$. In our computations, we neglect terms with $n \geq 40$ in Eqs. (1) and (3) which creates a truncation error of $O(10^{-5})$. For the purpose of comparison, droplet motion in a cylindrical tube is also computed. The radius of the cylinder is R, and the undisturbed flow far from the droplet is $u_x^\infty = 2U[1 - (y^2 + z^2)/R^2]$.

In the current paper, lengths are non-dimensionalized with R, velocities with the average channel velocity U and times with $\tau_f = R/U$. The droplet motion and deformation are affected by the capillary number defined as $Ca = \mu U/\gamma$, the viscosity ratio λ and the droplet size $a = \tilde{a}/R$. In addition, the deformation D for a droplet moving along the channel centerline is defined as the ratio of the droplet length l_x along the x-axis to the droplet length l_z along the z-axis, i.e., $D = l_x/l_z$.

2.2 Boundary integral formulation

Under low-Reynolds-number conditions, the motion of a viscous droplet in a micro-channel is governed by the Stokes equations and continuity. The velocity at a point $\boldsymbol{x}_0$ on the droplet interface S^d, the solid wall S^w or the fluid boundary S^f (as shown in Fig. 1) satisfies the following boundary integral equation

$$\begin{aligned}\Omega\boldsymbol{u}(\boldsymbol{x}_0) = &-\int_{S^d} [\boldsymbol{S}\cdot\Delta\boldsymbol{f} - \mu(1-\lambda)\boldsymbol{T}\cdot\boldsymbol{u}\cdot\boldsymbol{n}](\boldsymbol{x})\mathrm{d}S\\ &-\int_{S^w} \left[\boldsymbol{S}\cdot\boldsymbol{f}_2 - \mu\boldsymbol{T}\cdot\boldsymbol{u}_2\cdot\boldsymbol{n}\right](\boldsymbol{x})\mathrm{d}S\\ &-\int_{S^f} \left[\boldsymbol{S}\cdot\boldsymbol{f}_2 - \mu\boldsymbol{T}\cdot\boldsymbol{u}_2\cdot\boldsymbol{n}\right](\boldsymbol{x})\mathrm{d}S\end{aligned} \tag{4}$$

where Ω takes values $4\pi\mu(1+\lambda)$ and $4\pi\mu$ for $\boldsymbol{x}_0$ on S^d and the rest boundary, respectively, while the tensors $\boldsymbol{S}$ and $\boldsymbol{T}$ are known functions of position [5,23,37]. The boundary conditions on the droplet interface are

$$\boldsymbol{u} = \boldsymbol{u}_1 = \boldsymbol{u}_2 \tag{5}$$

$$\Delta\boldsymbol{f} \equiv \boldsymbol{f}_2 - \boldsymbol{f}_1 = \gamma(\nabla\cdot\boldsymbol{n})\boldsymbol{n} \tag{6}$$

where the subscripts “1” and “2” represent the flow inside the droplet and the suspending fluid, respectively. For the rest boundary, the following conditions apply

$$\boldsymbol{u} = 0 \text{ on solid surface } S^w \tag{7}$$

$$\boldsymbol{u} = \boldsymbol{u}^\infty \text{ on fluid surface } S^f \tag{8}$$

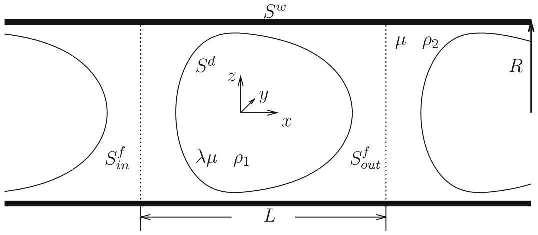

Fig. 2 Periodic conditions for an array of identical droplets separated by a distance L. Each droplet in the periodic cell is enclosed by the channel surface S^w, the fluid's inlet S^f_{in} and outlet S^f_{out}

2.3 Periodic boundary integral formulation

We illustrate in Fig. 2, the geometry of an array of identical droplets separated by a distance L in a square channel with size R. On the fluid boundaries S^f_{in} and S^f_{out}, periodic boundary conditions apply

$$\boldsymbol{u}_2^{\text{in}} = \boldsymbol{u}_2^{\text{out}} \qquad \text{and} \qquad \boldsymbol{f}_2^{\text{in}} - \boldsymbol{f}_2^{\text{out}} = \boldsymbol{\beta} \tag{9}$$

where $\boldsymbol{\beta} = \left(|\frac{\mathrm{d}p}{\mathrm{d}x}| L, 0, 0 \right)$. The superscripts "in" and "out" stand for the inlet and outlet of the fluid cell with length L, respectively, as shown in Fig. 2.

By expanding the third integral on the right-hand-side of Eq. (4) into a summation of the integral on the fluid inlet S^f_{in} and that on the fluid outlet S^f_{out}, and incorporating the periodic boundary conditions (9), Eq. (4) gives

$$\begin{aligned}\Omega \boldsymbol{u}(\boldsymbol{x}_0) = &- \int_{S^d} [\boldsymbol{S} \cdot \Delta \boldsymbol{f} - \mu(1-\lambda) \boldsymbol{T} \cdot \boldsymbol{u} \cdot \boldsymbol{n}] (\boldsymbol{x}) \mathrm{d}S \\ &- \int_{S^w} \left[\boldsymbol{S} \cdot \boldsymbol{f}_2 - \mu \boldsymbol{T} \cdot \boldsymbol{u}_2 \cdot \boldsymbol{n} \right] (\boldsymbol{x}) \mathrm{d}S \\ &- \int_{S^f_{\text{in}} \cup S^f_{\text{out}}} \left[\boldsymbol{S} \cdot \boldsymbol{f}_2 - \mu \boldsymbol{T} \cdot \boldsymbol{u}_2 \cdot \boldsymbol{n} \right] (\boldsymbol{x}) \mathrm{d}S \\ &+ \int_{S^f_{\text{in}}} [\boldsymbol{S} \cdot \boldsymbol{\beta}] (\boldsymbol{x}) \mathrm{d}S \end{aligned} \tag{10}$$

which may be employed to compute the motion of an array of droplets translating in a solid conduit with an arbitrary (constant) cross-sectional shape. The boundary conditions (5, 6, 7) also apply in this case.

2.4 Interfacial spectral boundary element method

Our three-dimensional spectral boundary element method (SBEM) is employed to solve numerically the aforementioned integral equations. More details on this methodology are provided in our earlier papers, e.g., [5,37]. For the completeness of the present study, in this section, we summarize our numerical method, address criteria for parameter selections and validate our numerical results.

The droplet interface, solid and fluid boundaries are divided into a moderate number N_E of surface elements which are parameterized by two variables ξ and η on the square interval $[-1, 1]^2$. The geometry and physical variables are discretized using Lagrangian interpolation in terms of these parametric variables. The N_B basis points (ξ_i, η_i) for the interpolation are chosen as the zeros of orthogonal polynomials of Gauss-type. This is equivalent to an orthogonal polynomial expansion and yields the spectral convergence associated with such expansions.

The boundary integral Eq. (4, 10) admit two different types of points. The collocation points $\boldsymbol{x}_0$ where the equations are required to hold and the basis points $\boldsymbol{x}$ where the physical variables $\boldsymbol{u}$ and $\boldsymbol{f}$ are specified or determined. Our spectral boundary element method employs collocation points $\boldsymbol{x}_0$ of Legendre–Gauss quadrature, i.e., in the interior of the elements. As a result the boundary integral equations hold even for singular elements, i.e., the elements that contain the corners of the channel geometry. (Similar approach has been utilized in our

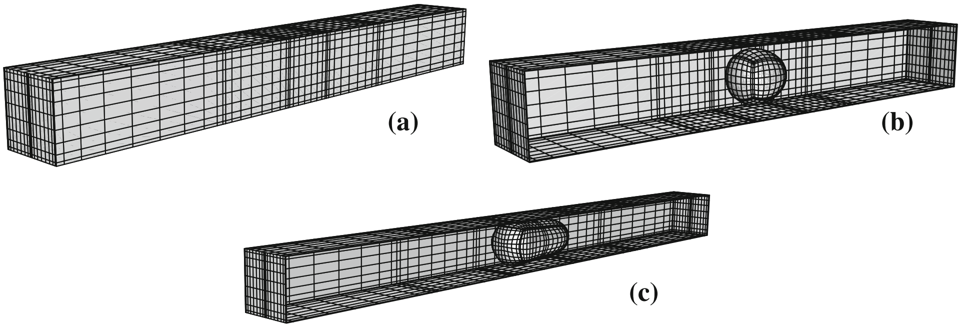

Fig. 3 Surface element discretization of **a** the channel wall where more elements are assigned on the area close to the droplet, **b** a slightly deformed droplet with 6 spectral elements and **c** a more elongated droplet with 10 spectral elements

earlier papers for droplets attached to solid surfaces and vascular endothelial cells or leukocytes adhering to the surface of blood vessels, e.g., [5,35,36].) In addition, we use basis points $\boldsymbol{x}$ of Legendre–Gauss–Lobatto quadrature, and thus, the physical variables are determined in the interior and on the edges of the spectral elements.

The discretization of the square channel and the droplet is demonstrated in Fig. 3. Seven rows with 4 elements each are employed on the channel wall. (Note that only five rows are shown in Fig. 3a). The total length of the channel/tube (which formally should extend to infinity) is 50 times of the drop length in the flow direction; this creates negligible error in all cases. For an array of identical droplets, the channel wall in each periodic cell is composed of 3 rows with 4 elements each; the length of the middle row is identical to the droplet length in the flow direction. For the discretization of the fluid boundary on the inlet and outlet of the channel, we utilize one, two or four elements; our computational results are identical and thus independent of the number of elements employed. For a droplet with size $\tilde{a} < R$, the droplet interface is divided into $N_E = 6$ elements as shown in Fig. 3b while the computations are initiated with a spherical shape. For a droplet with size $\tilde{a} > R$, the interface is divided into $N_E = 10$ elements as shown in Fig. 3c while the initial droplet shape is a prolate spheroid [33] having a length of $0.9R$ for the two minor semi-axes and a varying length for the major semi-axis (depending on the droplet volume).

In this study, we mainly used $N_B = 10$ basis points, i.e., $N_B \times N_B = 100$ spectral points on each spectral element. The accuracy of our results was verified by increasing the number of basis points for several characteristic cases involving small and large droplets. (The relative difference between the deformation for $N_B = 10$ and that for $N_B = 13$ was found to be $O(10^{-4})$.) For the time integration, we employed the 4th-order Runge–Kutta scheme with a typical time step $\Delta t = 5 \times 10^{-3}$. The problem studied in this paper admits three symmetry planes, $y = 0$, $z = 0$ and $y = z$. Exploiting these symmetries reduces the memory requirements for the storage of the system matrices by a factor of 8^2, the computational time for calculating the system matrices by a factor of 8 and the solution time of the linear systems via direct solvers by a factor of 8^3.

We have also validated our numerical results by comparing them with findings from earlier experimental and computational studies. Since most existing work for droplets in solid conduits is for cylindrical tubes, the comparisons that we performed are for droplets moving in a cylindrical tube. In those comparisons, we have used numerical schemes and discretizations similar to those for droplet motion in a square channel as discussed earlier. In particular, we have compared our results for single droplet motion in a cylindrical tube with those from the work of Tsai and Miksis [33], as shown in Fig. 4. Excellent agreement has been found by comparing our results (solid lines) to the axisymmetric computational results (points) in the literature. In addition, we have compared our results for a buoyant droplet rising in a cylindrical tube filled with another quiescent fluid with results obtained by Borhan and Pallinti [1], and for an array of identical droplets (i.e., under periodic boundary conditions) with the findings of Coulliette and Pozrikidis [4]. All comparisons with the earlier studies were in very good agreement as discussed in detail in the PhD thesis of Wang [34].

3 Motion of a single droplet

As soon as a droplet is released at the centerline of the square micro-channel, the droplet moves along the channel centerline and its shape deforms as shown in Fig. 5. Starting from an initial spherical shape for this case, the front region of the droplet becomes pointed while the rear flattened. Afterwards, the elongation of

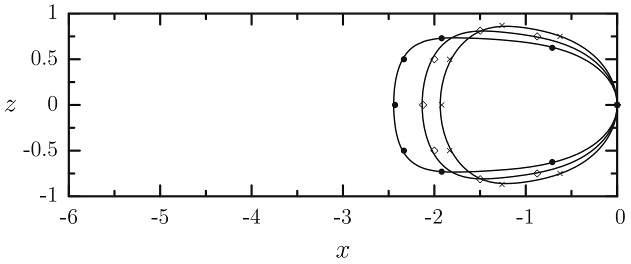

Fig. 4 The steady-state profile for a droplet with $a = 0.9$, $\lambda = 0.1$ and $Ca = 0.05, 0.1, 0.2$ (from *right* to *left*) traveling in a cylindrical tube. *Solid lines* represent results using our 3D spectral boundary element method, while the *crosses*, *open diamonds* and *solid circles* denote results taken from Tsai and Miksis [33]. The profiles are aligned at the droplet nose for convenience of comparison

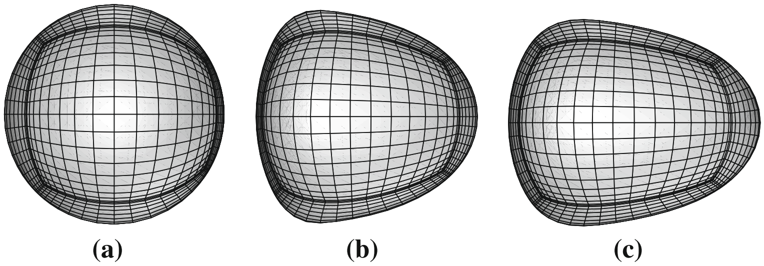

Fig. 5 Shape of a droplet with size $a = 0.914$ traveling in a square channel at time: **a** $t = 0$, **b** $t = 0.8$ and **c** $t = 12$. The viscosity ratio is $\lambda = 5$ and the capillary number is $Ca = 0.1$

the droplet body dominates the deformation and the droplet rear starts to regain some levels of the curvature. Finally, at steady state, the droplet interface shows a bullet-like shape with high curvature in the front region. This behavior is similar to that of a droplet moving in cylindrical tubes [11,19,33]. In this section, we investigate the influence of the droplet size a, capillary number Ca and viscosity ratio λ on the droplet deformation D and velocity U_x as well as the droplet-wall distance $h_{\min}$ for a single droplet in the square micro-channel. At the end of this section, we compare our results of a droplet moving in a square channel with those in a cylindrical tube.

3.1 Influence of the droplet size

The droplet dynamics in the channel is influenced significantly by the droplet size. To show this, in Fig. 6, we plot the time evolution of the droplet deformation D for sizes a ranged from 0.6 to 1.2 and capillary number $Ca = 0.1$. For a droplet with size smaller than the channel half-length (i.e., $a < 1$), we start our computations with a spherical droplet, while for droplets larger than the channel size (i.e., $a > 1$), the computations start with a prolate spheroid with two minor semi-axes equal to 0.9 and a suitable length for the major semi-axis to account for the droplet volume. We observe that for $a < 1$ the droplet deformation D increases with time and eventually reaches a plateau at steady sate. For $a > 1$, the deformation D decreases initially and then starts to gradually increase until a plateau is reached. The initial decrease in the deformation is due to the ellipsoidal assumption for the initial droplet shape for $a > 1$. For all droplet sizes, we find that smaller droplets achieve steady state faster with a smaller steady-state deformation than larger droplets. To visualize the steady-state shape, we plot in Fig. 7 the steady-state droplet profile and shape for different droplet sizes. Small droplets (e.g., $a = 0.6$) almost maintain the spherical shape throughout the course of their motion for the capillary number considered. Large droplets (e.g., $a = 1.0, 1.2$), on the other hand, experience stronger hydrodynamics forces in the thin lubrication film between the droplet interface and the wall, and thus, they show a significant elongation along the flow direction.

In Fig. 8, we plot the time evolution of the droplet velocity U_x in the flow direction for several droplet sizes. During the droplet translation, its velocity rapidly decreases to a minimum value upon release and then gradually increases to reach a plateau. The variation in velocity magnitude is more substantial for larger

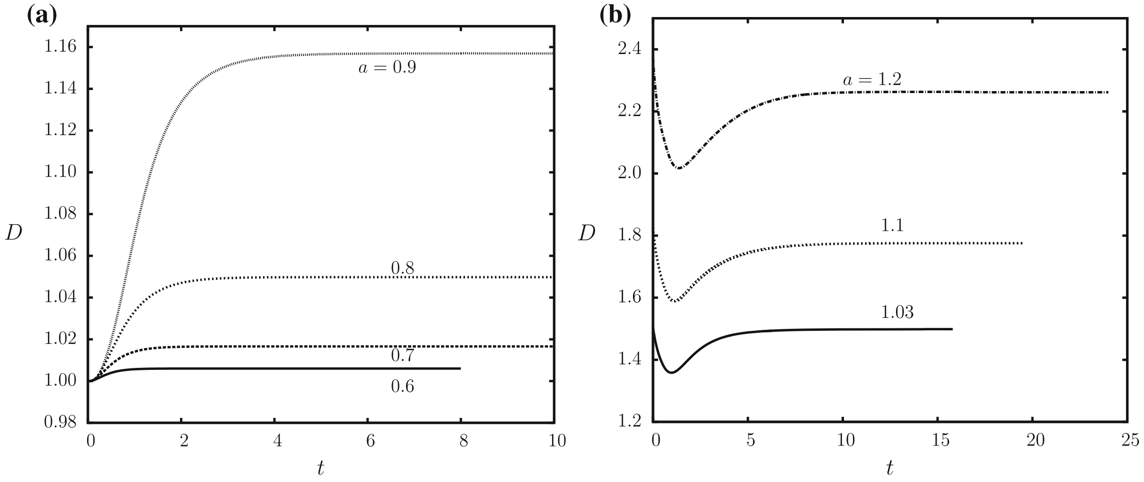

Fig. 6 Time evolution of the deformation D for a droplet with size **a** $a = 0.6, 0.7, 0.8, 0.9$ and **b** $a = 1.03, 1.1, 1.2$, for viscosity ratio $\lambda = 2.04$ and capillary number $Ca = 0.1$

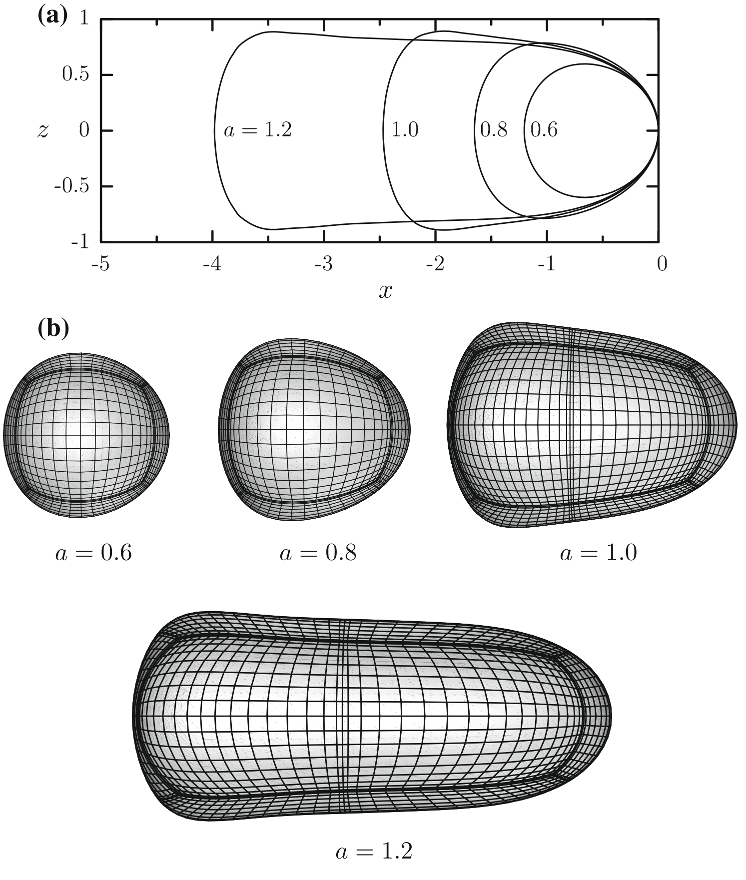

Fig. 7 **a** Steady-state droplet profile at the plane $y = 0$ for $a = 0.6, 0.8, 1.0, 1.2$. The profiles are aligned at the droplet nose for convenience of comparison. **b** The droplet shape for the same sizes a. The capillary number is $Ca = 0.1$ and the viscosity ratio is $\lambda = 2.04$

droplets. We also find that the steady-state droplet velocity decreases significantly with the increase in the drop size for small droplets ($a < 1$), while for droplets with a size similar or greater than the channel size, the droplet velocity increases slightly with the drop size.

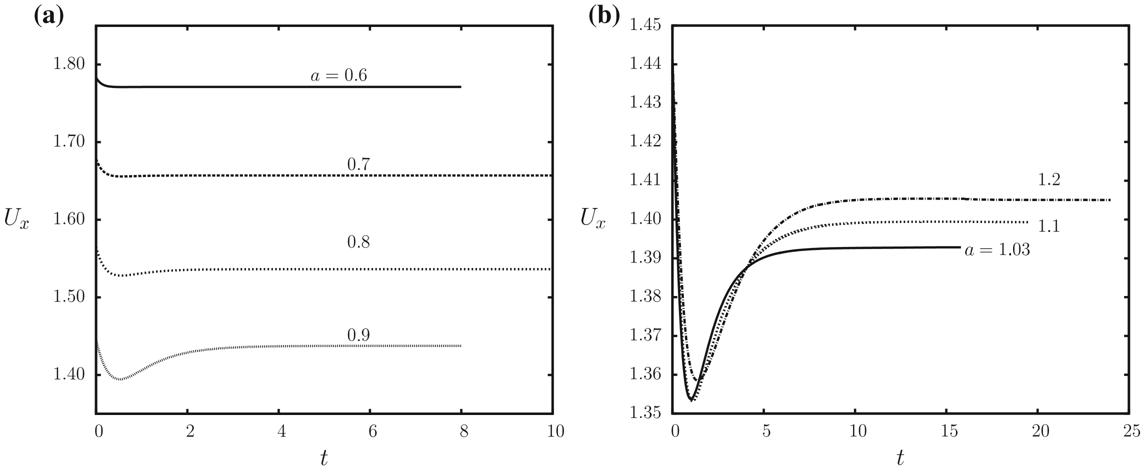

Fig. 8 Time evolution of the velocity U_x for a droplet with size **a** $a = 0.6, 0.7, 0.8, 0.9$ and **b** $a = 1.03, 1.1, 1.2$, for viscosity ratio $\lambda = 2.04$ and capillary number $Ca = 0.1$

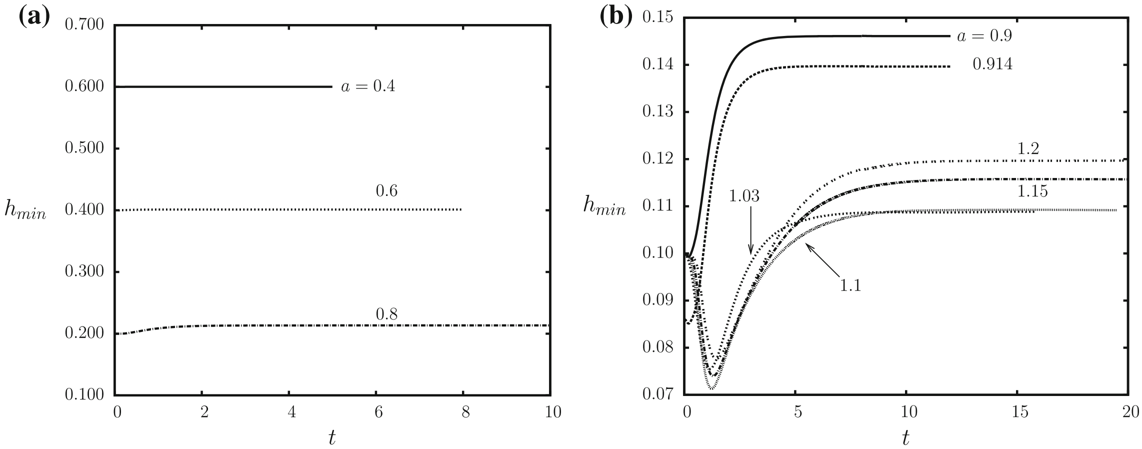

Fig. 9 Time evolution of the minimum droplet-wall distance $h_{\min}$ for a droplet with size **a** $a = 0.4, 0.6, 0.8$ and **b** $a = 0.9, 0.914, 1.03, 1.1, 1.15, 1.2$, for viscosity ratio $\lambda = 2.04$ and capillary number $Ca = 0.1$

The minimum distance (or gap) $h_{\min}$ between the droplet interface and the channel wall is plotted as a function of time in Fig. 9. For droplets much smaller than the channel size (i.e., $a \le 0.6$), the gap is practically constant over time. For larger droplets, the time evolution of the minimum gap is more complicated. For droplets with similar but smaller size than the channel (i.e., $a \le 1$), the minimum gap at steady state decreases with the droplet size, while for droplets with $a > 1$ the minimum steady-state gap increases with the droplet size owing to the higher interfacial deformation.

3.2 Influence of the capillary number

As a measure of the relative importance of deforming viscous forces to restoring surface tension forces on the droplet interface, the capillary number Ca influences substantially the behavior of the droplet in the channel. To show this, the time evolution of the droplet deformation D and velocity U_x are plotted in Fig. 10 for several capillary numbers Ca and for a droplet with size $a = 0.8$ (i.e., smaller than the channel size). As the flow rate Ca increases, the droplet needs more time to reach steady state and its final deformation is higher. After the droplet release in the channel, its velocity U_x instantly reaches a value greater than the average flow velocity in the channel (i.e., $U_x > 1$); then a minimum in U_x appears before the velocity starts to rapidly increase towards its steady-state value. Both the minimum and the steady-state velocity are increased with the capillary number. Similar behavior is observed for a droplet larger than the channel size as shown in Fig. 11 for droplet

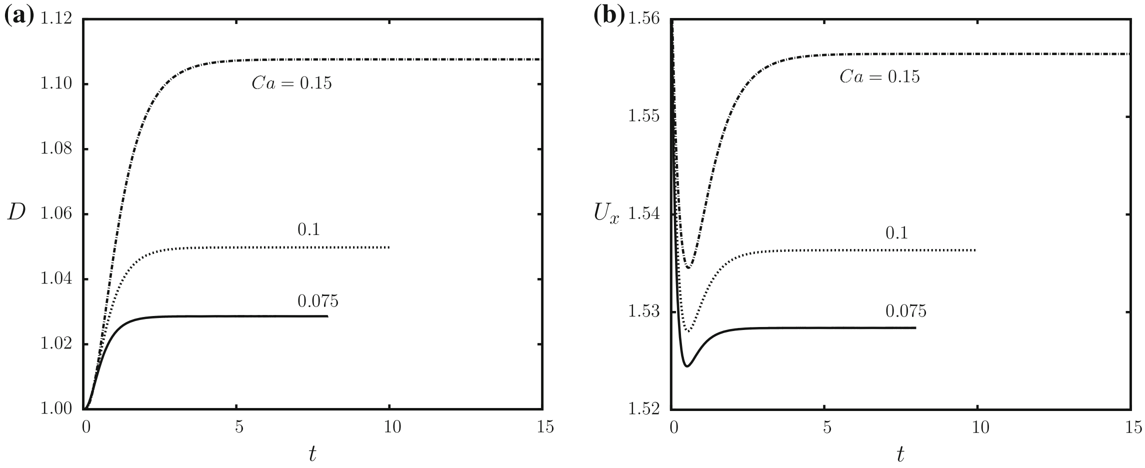

Fig. 10 Time evolution of **a** the deformation D and **b** the velocity U_x of a droplet with size $a = 0.8$ moving in a square channel, for capillary number $Ca = 0.075, 0.1, 0.15$ and viscosity ratio $\lambda = 2.04$

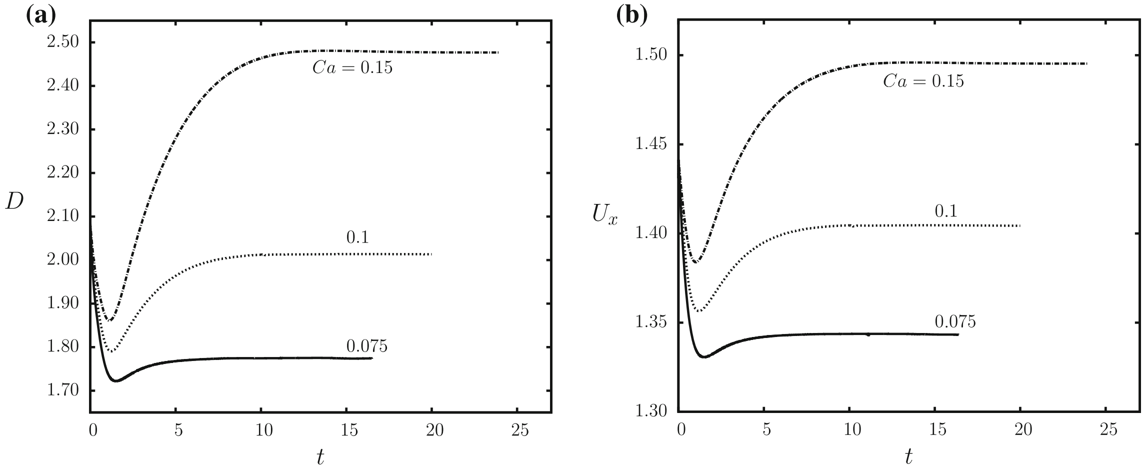

Fig. 11 Time evolution of **a** the deformation D and **b** the velocity U_x of a droplet with size $a = 1.15$, for capillary number $Ca = 0.075, 0.1, 0.15$ and viscosity ratio $\lambda = 2.04$

size $a = 1.15$. In this case, the initial decrease in deformation D results from the fact that the computations start with an ellipsoidal droplet shape.

Figure 12 shows the droplet profile at the plane $y = 0$ for several flow rates Ca for the two droplet sizes discussed earlier, i.e., $a = 0.8, 1.15$. As the capillary number increases, the droplet nose is more pointed, the droplet body is elongated and the rear is flattened. Comparison between different droplet sizes shows that the influence of the capillary number is more prominent for larger droplets which are substantially more elongated as shown in Fig. 12b.

Figure 13 shows the time evolution of the minimum distance $h_{\min}$ between the droplet interface and the channel wall for several flow rates Ca and for two droplet sizes $a = 0.8, 1.15$. For both droplets, the steady-state $h_{\min}$ increases with the capillary number owing to the higher interfacial deformation.

We collect now our steady-state results for the droplet deformation D, velocity U_x and minimum distance $h_{\min}$ as a function of the droplet size a for several flow rates Ca in Fig. 14. For small droplet sizes ($a \leq 0.6$), the steady-state deformation is almost independent of the droplet size and the capillary number; however, for larger droplets, the deformation increases substantially with the size a and the capillary number. As shown in Fig. 14b, the droplet velocity U_x at steady state decreases as the droplet size increases while practically a plateau is reached for larger droplets. The capillary number has almost no effects on the droplet velocity for small droplets ($a \leq 0.6$) but increases the velocity of large droplets. The minimum distance $h_{\min}$ between

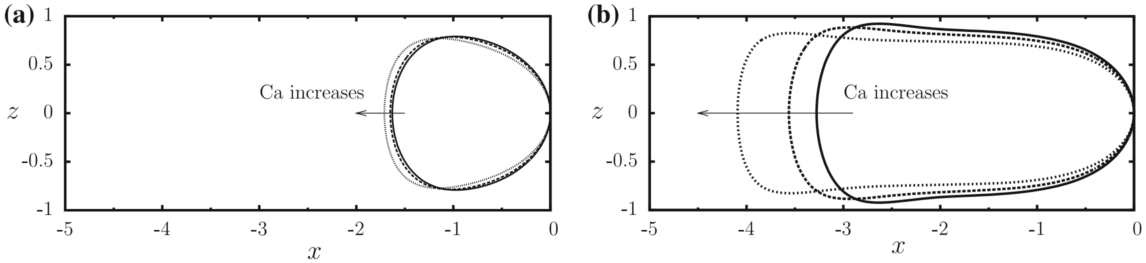

Fig. 12 Steady-state droplet profile with the plane $y = 0$ for capillary number $Ca = 0.075, 0.1, 0.15$ and viscosity ratio $\lambda = 2.04$. Droplet size: **a** $a = 0.8$ and **b** $a = 1.15$

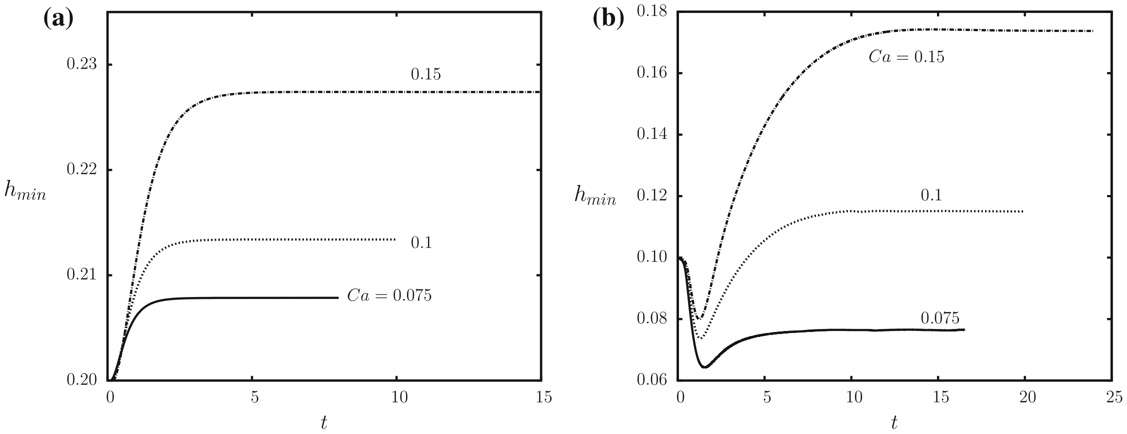

Fig. 13 Time evolution of the minimum distance $h_{\min}$ for droplet size **a** $a = 0.8$ and **b** $a = 1.15$, capillary number $Ca = 0.075, 0.1, 0.15$ and viscosity ratio $\lambda = 2.04$

the droplet interface and the channel wall shows a behavior similar to that of the droplet velocity as seen in Fig. 14c and becomes almost independent on the droplet size for large droplets.

3.3 Influence of the viscosity ratio

Figure 15 shows the transient evolution of the droplet deformation and velocity for different viscosity ratios. The droplet deformation initially experiences a sudden decrease; after a minimum is reached, the deformation increases and a plateau is formed at steady state. The aforementioned process takes place faster for a smaller viscosity ratio, i.e., a less viscous droplet spends less time deforming from its initial shape to its final configuration at steady state as expected since the time to reach steady state may be quantified as $\tau_f(1 + \lambda)$. The steady-state deformation is also higher for a larger viscosity ratio. The droplet velocity U_x is significantly influenced by the viscosity ratio λ and shows a monotonic decrease with the increase of λ.

The steady-state droplet profile at the plane $y = 0$ for several viscosity ratios are plotted in Fig. 16 for capillary number $Ca = 0.1$ and two droplet sizes $a = 0.8, 1.03$. For the smaller droplet, the droplet profile is not affected by the viscosity ratio even for the wide range of viscosity ratios considered here, i.e., $0.5 \leq \lambda \leq 10$. For the larger droplet, on the other hand, higher viscosity ratio causes a more pointed nose and greater elongation while a (slightly) thicker lubrication film is formed between the droplet and the channel wall as seen in Fig. 16b.

In Fig. 17, we plot the steady-state deformation D, velocity U_x and minimum droplet-wall distance $h_{\min}$ as a function of the droplet size a for two viscosity ratios. We find that D and $h_{\min}$ are independent of the viscosity ratio λ for small droplet size ($a \leq 0.7$) while both properties increase with the viscosity ratio for larger droplets owing to the higher interfacial deformation. On the contrary, the viscosity ratio has considerable effects on the steady-state droplet velocity U_x for all sizes; the droplet travels slower at steady state for higher viscosity ratio.

To further investigate the influence of the viscosity ratio, we plot the steady-state droplet deformation D and velocity U_x as a function of λ in Fig. 18, for a droplet with size $a = 0.914$ and capillary number $Ca = 0.1$.

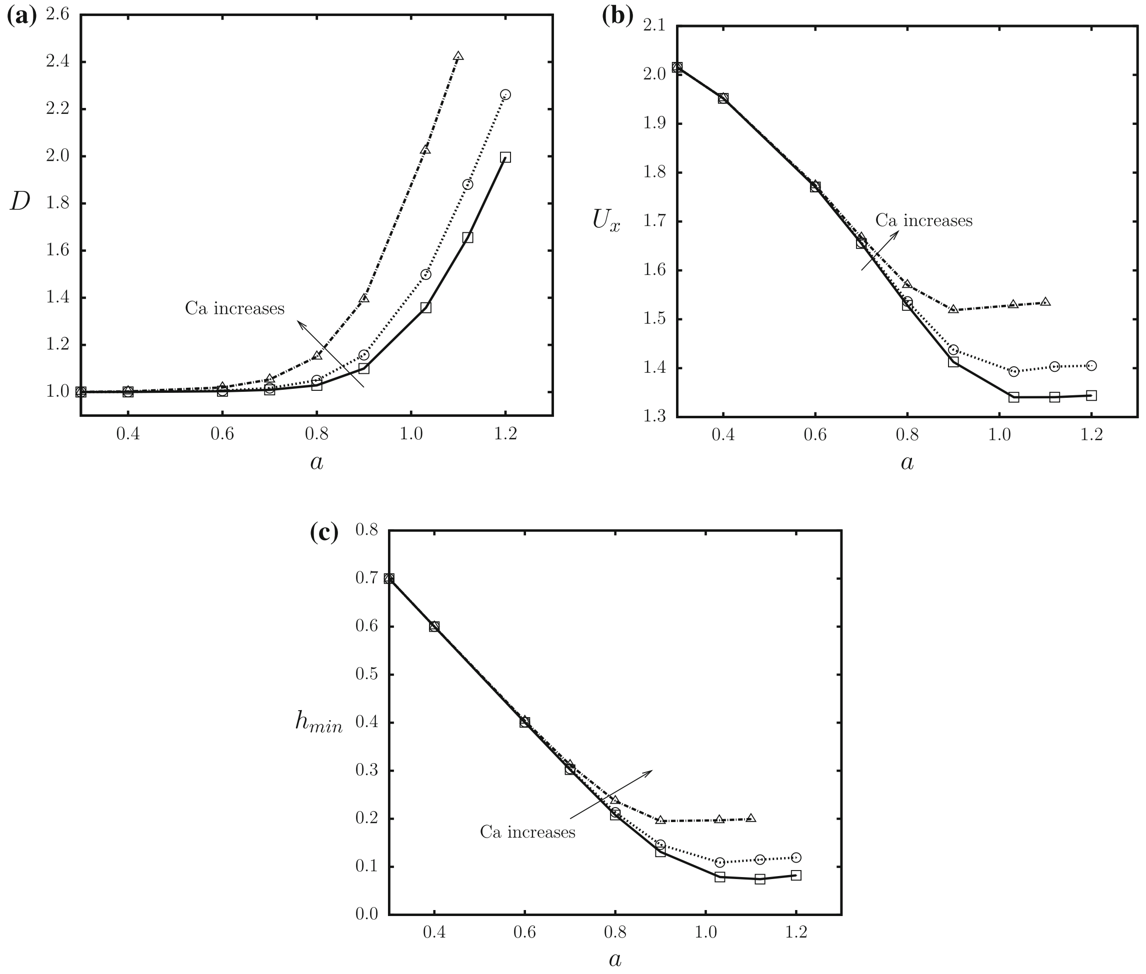

Fig. 14 **a** Droplet deformation D, **b** velocity U_x and **c** minimum droplet-wall distance $h_{\min}$ at steady state as a function of droplet size a for capillary number Ca: 0.075 (*squares*), 0.1 (*circles*) and 0.179 (*triangles*). The viscosity ratio is $\lambda = 2.04$

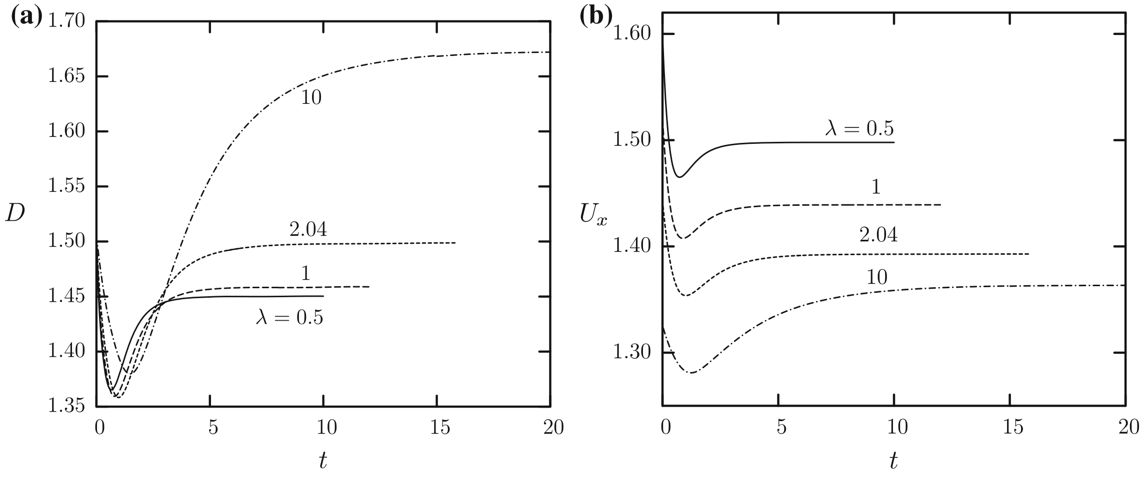

Fig. 15 Time evolution of **a** the deformation D and **b** the velocity U_x for a droplet with size $a = 1.03$ traveling in a square channel, for viscosity ratio $\lambda = 0.5$, 1, 2.04, 10 and capillary number $Ca = 0.1$

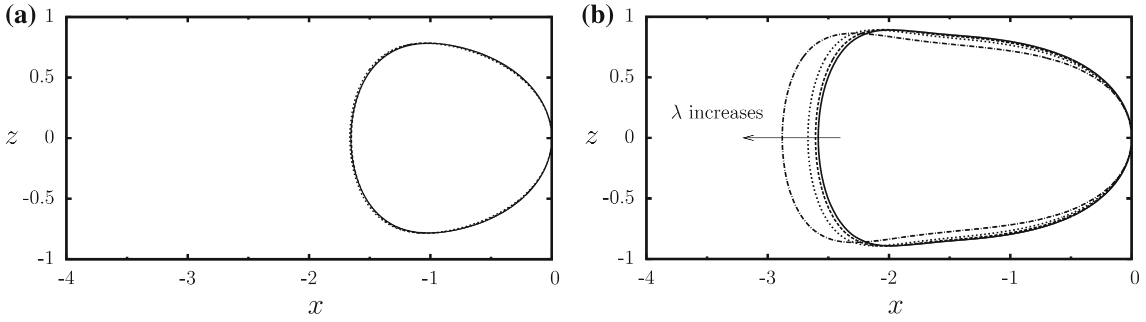

Fig. 16 Steady-state droplet profile for viscosity ratio $\lambda = 0.5, 1, 2.04, 10$ and capillary number $Ca = 0.1$. Droplet size: **a** $a = 0.8$, and **b** $a = 1.03$

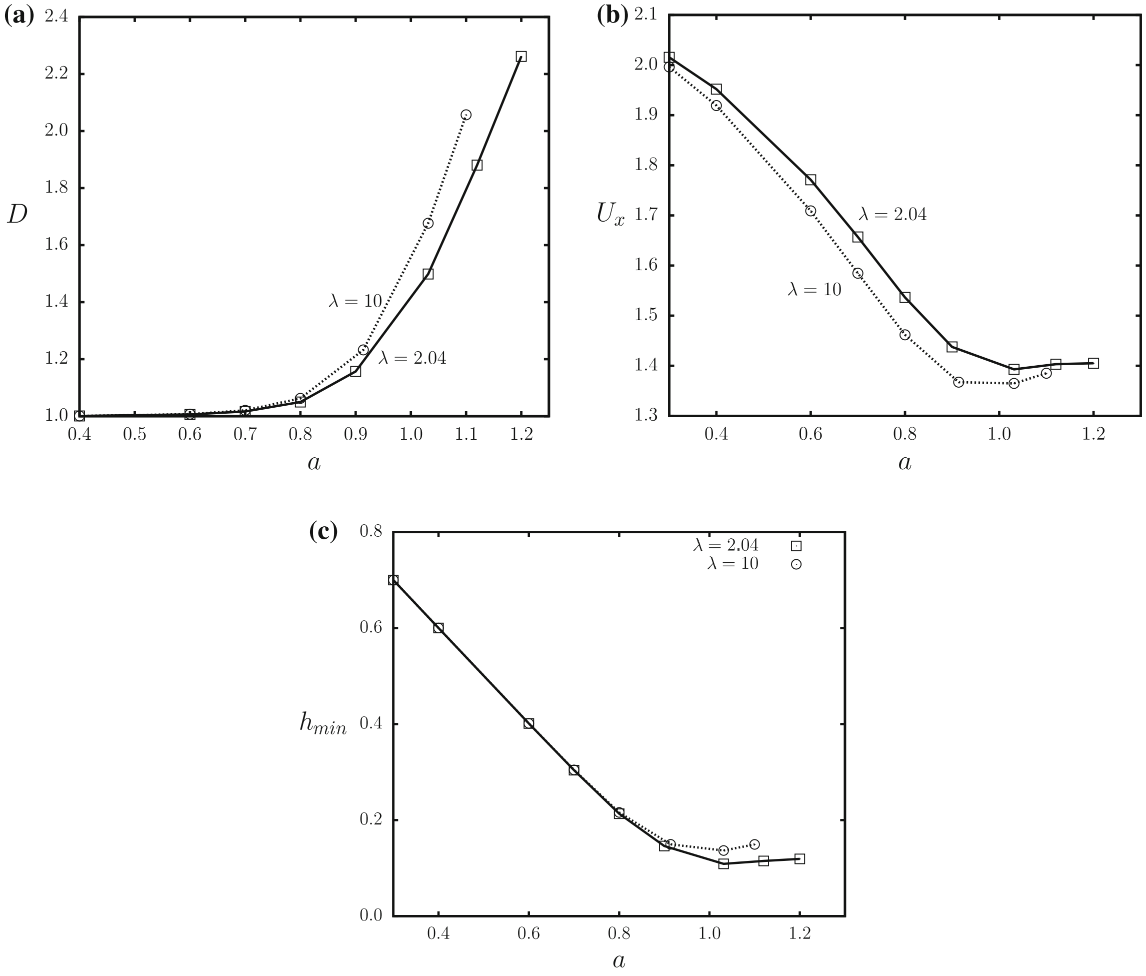

Fig. 17 **a** Deformation D, **b** velocity U_x and **c** minimum droplet-wall distance $h_{\min}$ at steady state as a function of the droplet size a, for viscosity ratio $\lambda = 2.04, 10$ and capillary number $Ca = 0.1$

The deformation D is found to increase with the viscosity ratio for $\lambda \geq 1$ while it is almost independent of the viscosity ratio for $\lambda < 1$. As shown in Fig. 18(b), the droplet velocity U_x decreases monotonically with the viscosity ratio. The influence of the viscosity ratio λ on the droplet deformation D and velocity U_x is qualitatively similar to that reported in the earlier experimental study of Ho and Leal [11] and the computations of Martinez and Udell [19] for a viscous drop moving in a cylindrical tube.

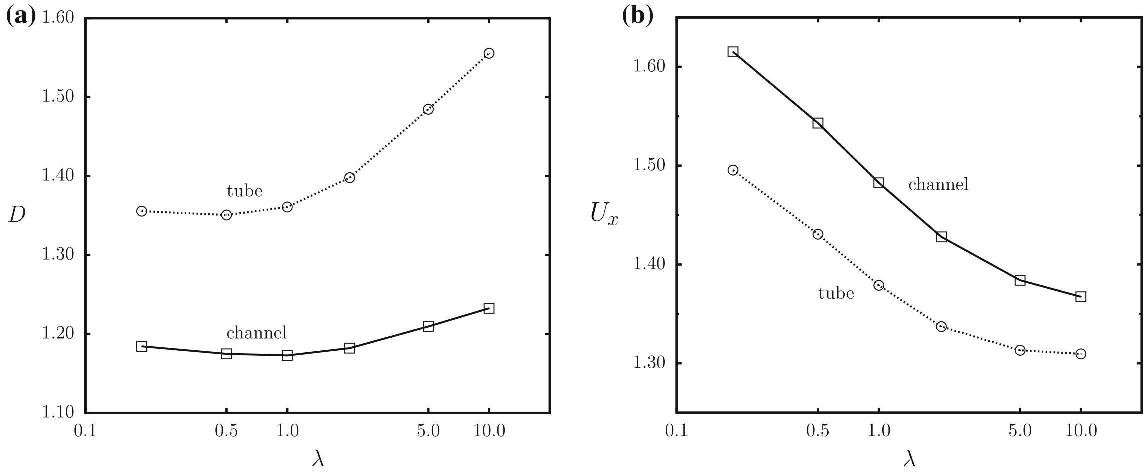

Fig. 18 **a** Droplet deformation D and **b** velocity U_x at steady state as a function of the viscosity ratio λ, for droplet size $a = 0.914$ and capillary number $Ca = 0.1$. Our results for a droplet translating in a cylindrical tube and a square channel are presented

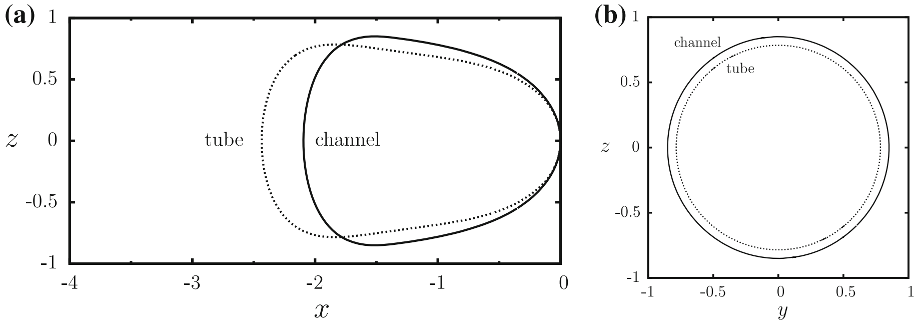

Fig. 19 Comparison of steady-state profiles for a droplet with size $a = 0.914$ in a cylindrical tube and a square channel, for capillary number $Ca = 0.1$ and viscosity ratio $\lambda = 10$. **a** Droplet profile at the plane $y = 0$. **b** Droplet profile at the plane $x = x_{\min}$ where the shortest droplet-wall distance occurs

3.4 Square channel versus cylindrical tube

For comparison with the droplet motion in a square micro-channel, we also calculate the droplet motion along the centerline of a cylindrical tube. In particular, in Fig. 18, we present the steady-state deformation and velocity for a droplet moving in a tube and a square channel as a function of the viscosity ratio, for droplet size $a = 0.914$ and capillary number $Ca = 0.1$. We note that the cross-section of the cylindrical tube subscribes that of the square channel while based on the definition of the capillary number used in this work, $Ca = \mu U/\gamma$, the same capillary number means that for the same droplet the average velocity U is the same for both solid ducts. The droplet experiences a higher deformation and a smaller velocity in the tube for a given viscosity ratio. The smaller interfacial deformation in the channel results from the existence of the corners' area which permits flow of the surrounding fluid and thus causes less deformation on the droplet.

Figure 19a shows the steady-state droplet profile at the plane $y = 0$ in a square channel and a cylindrical tube. A much elongated and tapered droplet profile is found in the tube flow. Fig. 19b shows the droplet profile at plane $x = x_{\min}$ where the shortest distance between the droplet interface and the solid wall occurs. At this location, we found that droplet blocks nearly 57% of the cross-sectional area of the channel and 62% of the cross-sectional area of the tube. The smaller area that the droplet blocks in the channel flow may result in a higher droplet velocity in this duct shown earlier in Fig. 18b.

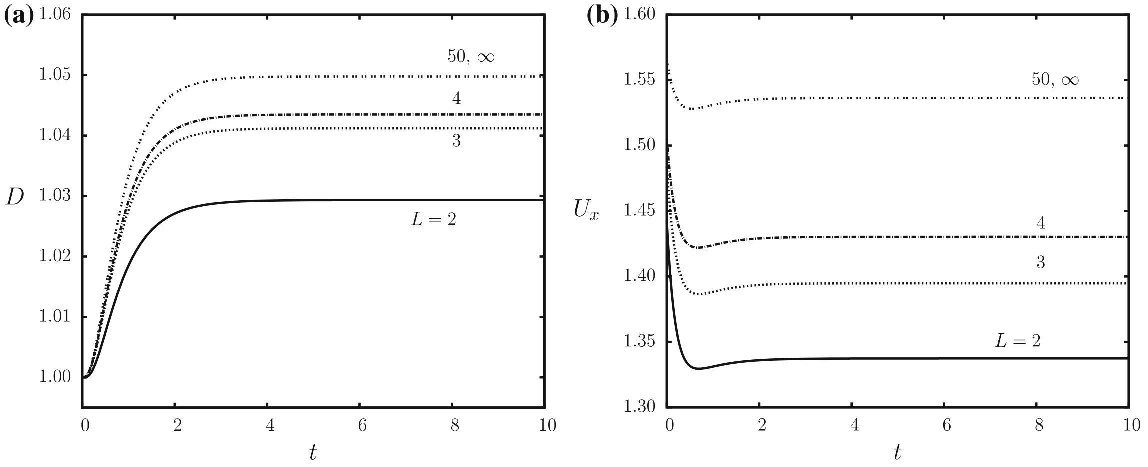

Fig. 20 Time evolution of **a** the deformation D and **b** the velocity U_x for an array of droplets with separation distance $L = 2, 3, 4, 50, \infty$ traveling in a square channel. The droplet size is $a = 0.8$, the capillary number is $Ca = 0.1$ and the viscosity ratio is $\lambda = 2.04$

4 A periodic array of droplets moving in a channel

When an array of droplets move in a channel, the deformation and velocity of a given droplet may be affected by its neighboring droplets, and thus, the droplets separation distance L (shown earlier in Fig. 2) plays an important role. When the droplets distance L is small, the periodic droplet motion may deviate from that of a single droplet; as the droplets distance L approaches infinity (i.e., becomes large enough), the periodic droplet behaves like a single droplet in the channel. In this study, we assume that the droplets in the array have identical properties including size, surface tension and viscosity. Thus, the periodic boundary integral formulation is employed as discussed in Sect. 2.3.

Figure 20 shows the time evolution of the deformation D and the velocity U_x for droplets separation $L = 2, 3, 4, 50, \infty$, droplet size $a = 0.8$ and capillary number $Ca = 0.1$. The existence of closer neighboring droplets incurs a reduced deformation and smaller velocity for each droplet. We also include in this figure the deformation and velocity of a single droplet (i.e., for $L \to \infty$) with the same capillary number and viscosity ratio and find the results are identical to those for $L = 50$ as expected owing to the large droplets separation.

For a larger value of the capillary number, $Ca = 0.179$, and separation $L = 2, \infty$, we plot the time evolution of the deformation and droplet velocity in Fig. 21. The corresponding steady-state droplet shapes and profiles are shown in Fig. 22. Clearly, a droplet with nearer neighbors tends to form a less pointed nose and show a smaller deformation, while it moves slower than a single droplet in the channel. We also notice by comparing Figs. 20 and 21 that the difference in the deformation D and velocity U_x between different separation distances L may vary depending on the capillary number Ca. As shown in Fig. 23, we plot the relative difference in droplet deformation and velocity between separations $L = 2$ and $L \to \infty$ as a function of capillary number Ca. As Ca increases, the relative different in deformation increases while that in droplet velocity decreases slightly. This implies that with higher flow rate of the suspending fluid or more deformable droplet interface, the droplets experience noticeably larger deformation for larger separations.

Similarly, we investigate the influence of viscosity ratio on the difference in the droplet behavior between different separation distances. Figure 24 shows the relative differences in droplet deformation and velocity between separations $L = 2$ and $L \to \infty$ as a function of viscosity ratio λ. The differences in both deformation and velocity increase with the viscosity ratio, while the increase in the velocity difference is much more significant. The results indicate that for more viscous droplets, the droplet velocity is much more reduced when the droplets are traveling with a smaller separation distance.

We consider now the periodic motion of larger droplets with size $a = 1.2$. The time evolution of the deformation D and velocity U_x for separation distance $L = 4.5, \infty$ and capillary number $Ca = 0.1$ are shown in Fig. 25, while the corresponding interfacial shapes and profiles at steady state are presented in Fig. 26. A substantial reduction in the droplet deformation and velocity is observed when the droplets are closely located. It is interesting to note that for separation $L = 4.5$ (where the droplets travel quite close together as seen in Fig. 26), their velocity is very close to the channel's average velocity U. In Fig. 27, we plot the relative

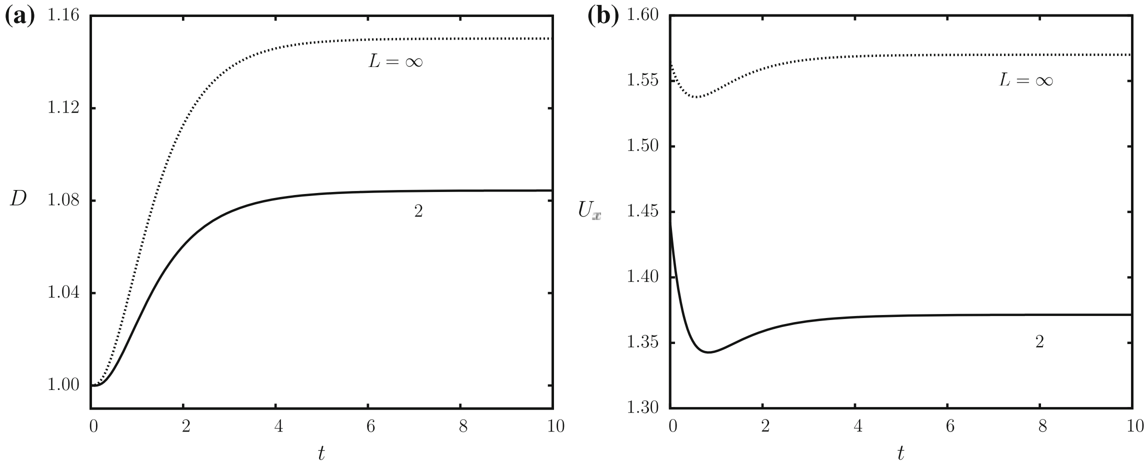

Fig. 21 Time evolution of **a** the deformation D and **b** the velocity U_x for an array of droplets with separation distance $L = 2, \infty$ traveling in a square channel. The droplet size is $a = 0.8$, the capillary number is $Ca = 0.179$ and the viscosity ratio is $\lambda = 2.04$

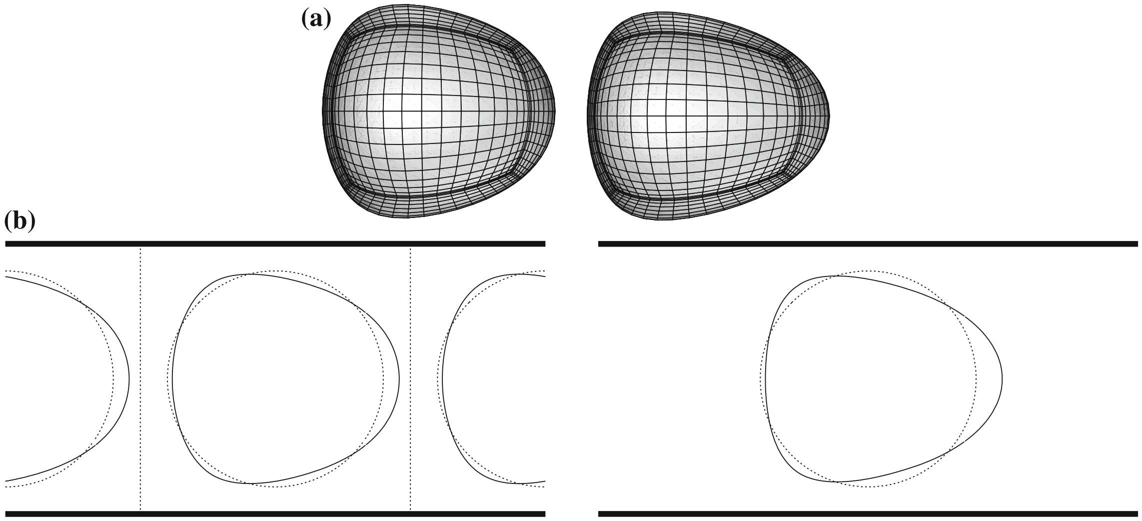

Fig. 22 **a** Steady-state droplet shape and **b** profile at the plane $y = 0$, for an array of droplets with size $a = 0.8$ and separation distance $L = 2$ (*left*) and $L \to \infty$ (*right*) traveling in a square channel, for capillary number $Ca = 0.179$ and viscosity ratio $\lambda = 2.04$. In **b**, for both separation distances, the steady-state profile (*solid curve*) of the droplet is compared with its initial profile *(dotted curve)*

difference in the steady-state droplet deformation and velocity between separations $L = 4.5$ and $L \to \infty$ as a function of droplet size a. For both the deformation and the velocity, significant increase is observed for the difference between the two separations as we increase the droplet size. The magnitude of the increase in the differences are much larger than those incurred by varying Ca and λ. We conclude that the reduction in droplet deformation and velocity as a result of small droplet-to-droplet separation distance is influenced by the capillary number Ca, viscosity ratio λ and more significantly the droplet size a.

5 Conclusions

In this study, we have investigated computationally the low-Reynolds-number droplet motion in a square micro-channel, a problem frequently encountered in microfluidic devices, enhanced oil recovery and coating processes [15,17,30]. The droplet deformation and motion were determined via our three-dimensional spectral boundary element method for wall-bounded flows [37].

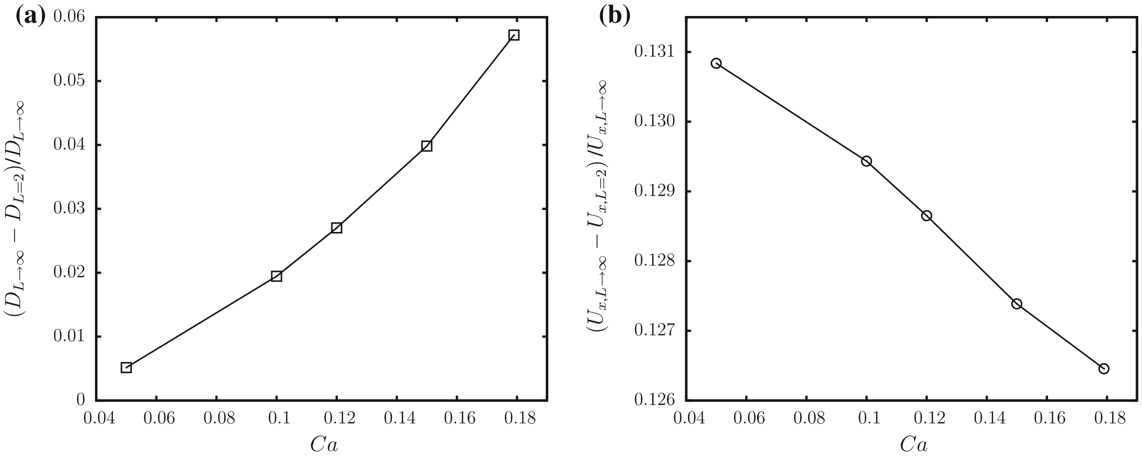

Fig. 23 Relative differences in steady-state **a** droplet deformation and **b** velocity between $L = 2$ and $L \to \infty$ as a function of capillary number Ca. The droplet size is $a = 0.8$ and the viscosity ratio is $\lambda = 2.04$

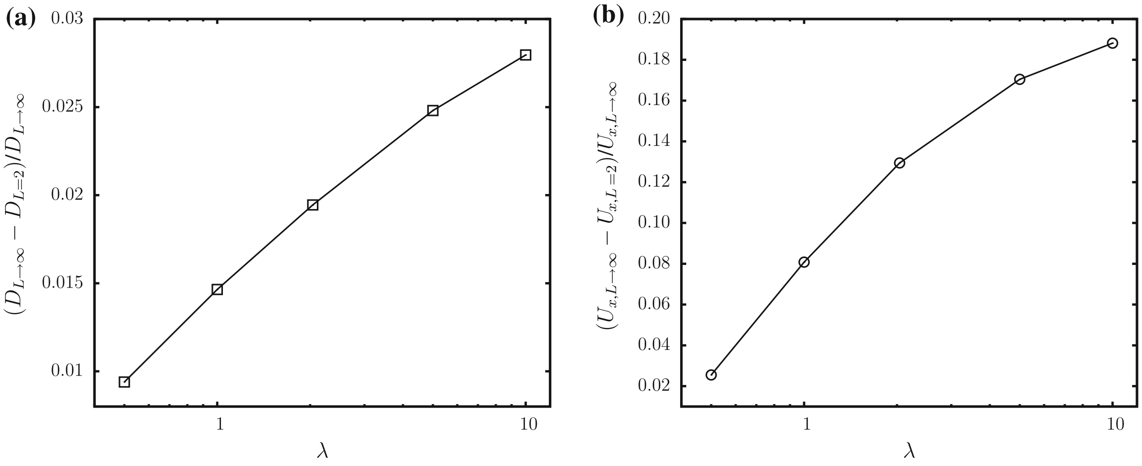

Fig. 24 Relative differences in steady-state **a** droplet deformation and **b** velocity between $L = 2$ and $L \to \infty$ as a function of viscosity ratio λ. The droplet size is $a = 0.8$ and the capillary number is $Ca = 0.1$

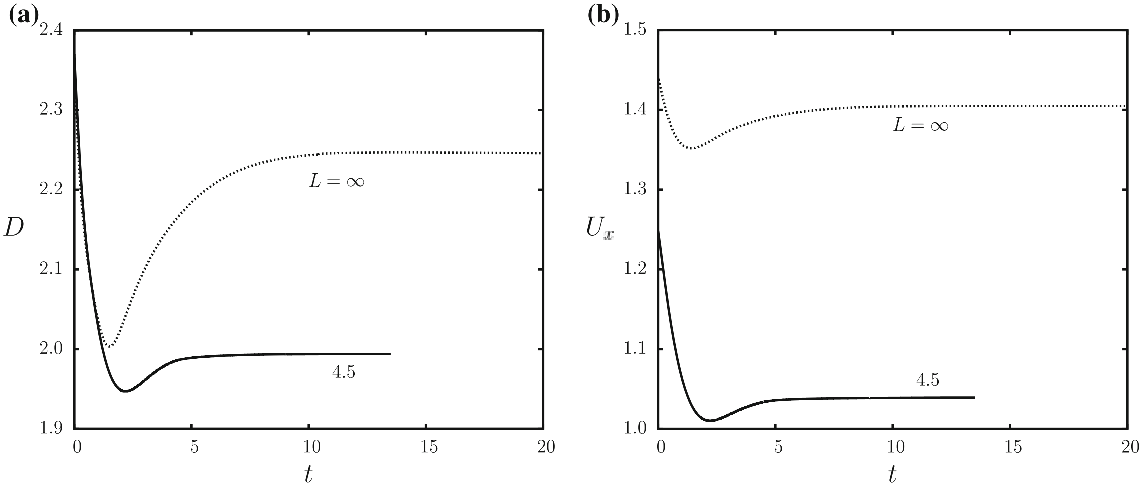

Fig. 25 Time evolution of **a** the deformation D and **b** the velocity U_x for an array of droplets with separation distance $L = 4.5, \infty$ traveling in a square channel. The droplet size is $a = 1.2$, the capillary number is $Ca = 0.1$ and the viscosity ratio is $\lambda = 2.04$

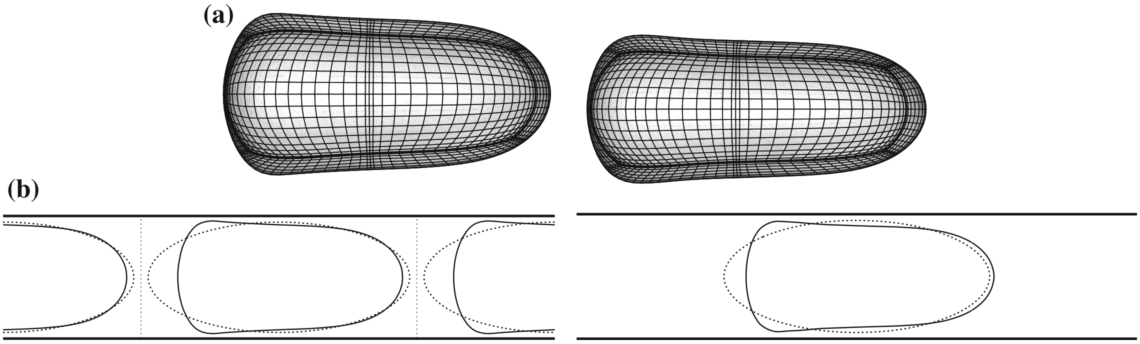

Fig. 26 **a** Steady-state droplet shape and **b** profile at the plane $y = 0$, for an array of droplets with size $a = 1.2$ and separation distance $L = 4.5$ (*left*) and $L \to \infty$ (*right*) traveling in a square channel, for capillary number $Ca = 0.1$ and viscosity ratio $\lambda = 2.04$. In **b**, for both separation distances, the steady-state profile (*solid curve*) of the droplet is compared with its initial profile (*dotted curve*)

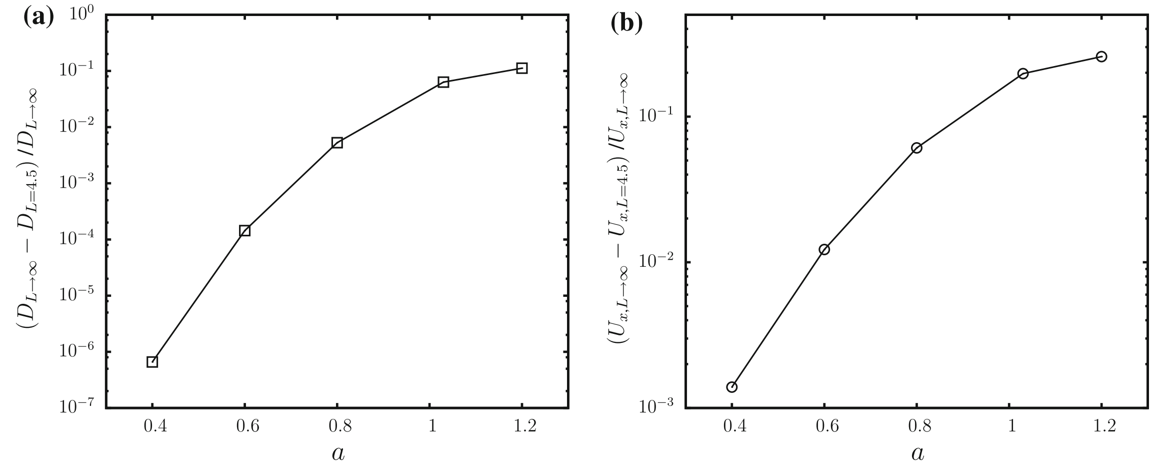

Fig. 27 Relative differences in steady-state **a** droplet deformation and **b** velocity between $L = 4.5$ and $L \to \infty$ as a function of droplet size a. The capillary number is $Ca = 0.1$ and the viscosity ratio is $\lambda = 2.04$

For single droplet motion in a square micro-channel, the effects of the flow rate (or capillary number Ca), viscosity ratio λ and droplet size a on the interfacial dynamics were identified for droplets smaller and larger than the channel size and for a wide range of viscosity ratio. Owing to the stronger hydrodynamic forces in the thin lubrication film between the droplet interface and the solid walls, large droplets exhibit higher deformation and smaller velocity for a given flow rate. In addition, the influence of the capillary number on the droplet shape is more prominent for large droplets. As the viscosity ratio increases, the droplet velocity is decreased and its deformation is increased for $\lambda \geq 1$ while for $\lambda < 1$, the droplet deformation is practically independent of λ. Under the same average velocity, a droplet in a channel shows a significantly lower deformation and higher velocity than in a cylindrical tube with the same size, owing to the existence of the corners' area in the channel which permits flow of the surrounding fluid.

Periodic boundary conditions have been incorporated into our spectral boundary element algorithm and used to study the dynamics of an array of identical droplets moving in the channel. In this case, the droplet deformation and velocity are reduced as their separation decreases; the reduction is influenced by the capillary number Ca, viscosity ratio λ and more significantly the droplet size a.

The current computational study demonstrates the capability of our three-dimensional spectral boundary element method [37] to determine droplet motion in microfluidic channels. The incorporation of periodic boundary conditions allows the investigation of an array of identical droplets in straight solid ducts. With further modification of the solid geometry, more complicated droplet dynamics may be considered, e.g., droplet motion in cross- or T-junctions.

Acknowledgments This work was supported in part by the National Science Foundation and the Department of Energy (Award #DE-FG52-08NA28921). Acknowledgment is also made to the donors of the American Chemical Society Petroleum Research Fund for partial support of this research. Most computations were performed on multiprocessor computers provided by the National Center for Supercomputing Applications (NCSA) in Illinois. Some computations were carried out on high performance computing systems at the Center for Computationally Assisted Science & Technology (CCAST) at North Dakota State University.

References

1. Borhan, A., Pallinti, J.: Buoyancy-driven motion of viscous drops through cylindrical capillaries at small Reynolds numbers. Ind. Eng. Chem. Res. **34**, 2750–2761 (1995)
2. Bretherton, F.P.: The motion of long bubbles in tubes. J. Fluid Mech. **10**, 166–188 (1961)
3. Chen, J.D.: Measuring the film thickness surrounding a bubble inside a capillary. J. Colloid Interface Sci. **109**, 314–349 (1986)
4. Coulliette, C., Pozrikidis, C.: Motion of an array of drops through a cylindrical tube. J. Fluid Mech. **358**, 1–28 (1998)
5. Dimitrakopoulos, P., Higdon, J.J.L.: On the displacement of three-dimensional fluid droplets from solid surface in low-Reynolds-number shear flows. J. Fluid Mech. **377**, 189–222 (1998)
6. Fair, R.B.: Digital microfluidics: is a true lab-on-a-chip possible? Microfluid Nanofluid **3**, 245–281 (2007)
7. Giavedoni, M.D., Saita, F.A.: The axisymmetric and plane cases of a gas phase steadily displacing a newtonian liquid—a simultaneous solution of the governing equations. Phys. Fluids **9**, 2420–2428 (1997)
8. Giavedoni, M.D., Saita, F.A.: The rear meniscus of a long bubble steadily displacing a newtonian liquid in a capillary tube. Phys. Fluids **11**, 786–794 (1999)
9. Griggs, A.J., Zinchenko, A.Z., Davis, R.H.: Low-Reynolds-number motion of a deformable drop between two parallel plane walls. Int. J. Multiph. Flow **33**, 182–206 (2007)
10. Hazel, A.L., Heil, M.: The steady propagation of a semi-infinite bubble into a tube of elliptical or rectangular cross-section. J. Fluid Mech. **470**, 91–114 (2002)
11. Ho, B.P., Leal, L.G.: The creeping motion of liquid drops through a circular tube of comparable diameter. J. Fluid Mech. **71**, 361–383 (1975)
12. Hodges, S.R., Jensen, O.E., Rallison, J.M.: The motion of a viscous drop through a cylindrical tube. J. Fluid Mech. **501**, 279–301 (2004)
13. Janssen, P.J.A., Anderson, P.D.: Boundary-integral method for drop deformation between parallel plates. Phys. Fluids **19**, 043, 602 (2007)
14. Janssen, P.J.A., Anderson, P.D.: A boundary-integral model for drop deformation betwee two parallel plates with non-unit viscosity ratio drops. J. Comput. Phys. **227**, 8807–8819 (2008)
15. Kolb, W.B., Cerro, R.L.: Coating the inside of a capillary of square cross section. Chem. Eng. Sci. **46**, 2181–2195 (1991)
16. Kolb, W.B., Cerro, R.L.: The motion of long bubbles in tubes of square cross section. Phys. Fluids A **5**, 1549–1557 (1993)
17. Link, D.R., Anna, S.L., Weitz, D.A., Stone, H.A.: Geometrically mediated breakup of drops in microfluidic devices. Phys. Rev. Lett. **92**, 054, 503 (2004)
18. Lu, G.Q., Wang, C.Y.: Electrochemical and flow characterization of a direct methanol fuel cell. J. Power Sources **134**, 33–40 (2004)
19. Martinez, M.J., Udell, K.S.: Axisymmetric creeping motion of drops through circular tubes. J. Fluid Mech. **210**, 565–591 (1990)
20. Mortazavi, S., Tryggvason, G.: A numerical study of the motion of drops in poiseuille flow. Part 1. Lateral migration of one drop. J. Fluid Mech. **411**, 325–350 (2000)
21. Olbricht, W.: Pore-scale prototypes of multiphase flow in porous media. Ann. Rev. Fluid Mech. **28**, 187–213 (1996)
22. Olbricht, W.L., Kung, D.M.: The deformation and breakup of liquid drops in low Reynolds number flow through a capillary. Phys. Fluids A **4**, 1347–1354 (1992)
23. Pozrikidis, C.: Boundary Integral and Singularity Methods for Linearized Viscous Flow. Combridge University Press, Cambridge (1992)
24. Ransohoff, T.C., Radke, C.J.: Weeping flow around nonwetting bubbles trapped in constricted noncircular pores. Physico-Chem. Hydrodyn **8**, 255–263 (1987)
25. Ratulowski, J., Chang, H.: Transport of gas bubbles in capillaries. Phys. Fluids A **1**, 1642–1655 (1989)
26. Sarrazin, F., Bonometti, T., Prat, L., Gourdon, C., Magnaudet, J.: Hydrodynamic structures of droplets engineered in rectangular micro-channels. Microfluid Nanofluid **5**, 131–137 (2008)
27. Shapira, M., Haber, S.: Low Reynolds number motion of a droplet in shear flow including wall effects. Int. J. Multiph. Flow **16**, 305–321 (1990)
28. Shen, E.I., Udell, K.S.: A finite element study of low Reynolds number two-phase flow in cylindrical tubes. Trans. ASME: J. Appl. Mech. **52**, 253–256 (1985)
29. Song, H., Tice, J.D., Ismagilov, R.F.: A microfluidic system for controlling reaction networks in time. Angew. Chem. Int. Ed. **42**, 767–772 (2003)
30. Tan, Y., Fisher, J.S., Lee, A.I., Cristini, V., Lee, A.P.: Design of microfluidic channel geometries for the control of droplet volume, chemical concentration, and sorting. Lab Chip **4**, 292–298 (2004)
31. Teh, S.Y., Lin, R., Hung, L.H., Lee, A.P.: Droplet microfluidics. Lab Chip **8**, 198–220 (2008)
32. Thulasidas, T.C., Abraham, M.A., Cerro, R.L.: Bubble-train flow in capillaries of circular and square cross section. Chem. Eng. Sci. **50**, 183–199 (1995)
33. Tsai, T.M., Miksis, M.J.: Dynamics of a drop in a constricted capillary tube. J. Fluid Mech. **274**, 197–217 (1994)
34. Wang, Y.: Flow and interfacial dynamics in vascular vessels and microfluidics. PhD. Thesis, University of Maryland (2007)
35. Wang, Y., Dimitrakopoulos, P.: Nature of the hemodynamic forces exerted on vascular endothelial cells or leukocytes adhering to the surface of blood vessels. Phys. Fluids **18**, 087, 107 (2006)

36. Wang, Y., Dimitrakopoulos, P.: Normal force exerted on vascular endothelial cells. Phys. Rev. Lett. **96**, 028, 106 (2006)
37. Wang, Y., Dimitrakopoulos, P.: A three-dimensional spectral boundary element algorithm for interfacial dynamics in stokes. Phys. Fluids **18**, 082, 106 (2006)
38. Wong, H., Radke, C.J., Morris, S.: The motion of long bubbles in polygonal capillaries. Part 1. Thin films. J. Fluid Mech. **292**, 71–94 (1995)
39. Wong, H., Radke, C.J., Morris, S.: The motion of long bubbles in polygonal capillaries. Part 2. Drag, fluid pressure and fluid flow. J. Fluid Mech. **292**, 95–110 (1995)
40. Yih, C.S.: Fluid Mechanics. West River Press, Ann Arbor (1979)